

## **Evaluation of Macroscopic Elastic Properties of Porous Compacts Prepared by Powder Pressure Sintering for Biomedical Implant\***

Isao TAGUCHI\*\* and Michio KURASHIGE\*\*\*

\*\* Graduate School of Engineering, Iwate University,

Ueda 4-3-5, Morioka-shi, Iwate 020-8551, Japan.

E-mail: isao\_taguchi@pref.aomori.lg.jp

\*\*\* Department of Mechanical Engineering, Iwate University,

Ueda 4-3-5, Morioka-shi, Iwate 020-8551, Japan.

### **Abstract**

Macroscopic elastic properties of porous compacts prepared by applying uniaxial pressure in powder sintering are numerically estimated, with their biomedical application in mind. The estimation is based on a three step simulation method similar to the previous one. It is found that the compaction by the pressure and the sintering lead to increase in the macroscopic elastic moduli in the pressure direction, which is made to coincide with that of gravity in packing. It is also found that these moduli are larger than those in the direction normal to the pressure by 20% to 40%. Those for the less sintered compacts whose porosity ranges from approximately 32% to 37% fall in those of human cortical bone and show similar behavior to those of artificial implants.

**Key words:** Powder Compaction; Simulation; Elastic Modulus; Anisotropy; Human Bone

### **1. Introduction**

Titanium and its alloys are currently widely used as structural biomaterials for replacement of hard tissues by devices such as artificial hip joints and dental implants, because they have excellent specific strength and corrosion resistance and furthermore they have the best biocompatibility characteristics among metallic biomaterials<sup>(1),(2)</sup>. However, the critical problem concerning metallic implants in orthopedic surgery is the mismatch of Young's modulus between the bone and metallic implants. One way to alleviate the problem is to reduce Young's modulus of metallic materials by introducing pores. An additional advantage of this way is that bone-implant fixation is achieved by interdigitation between the bone and porous implant matrix<sup>(3)</sup>.

Using pure Ti powder of particles with 45 to 500  $\mu$  m in diameter prepared by the plasma rotating electrode process, Oh et al.<sup>(4),(5)</sup> proposed porous pure Ti compacts synthesized by powder sintering. The porous compacts having porosity of 5.0% to 37.1% are successfully fabricated by controlling sintering condition<sup>(5)</sup>. It was found that Young's modulus decreases linearly with increasing porosity, and porous Ti compacts having porosity of approximately 32% to 36% exhibit Young's modulus equivalent to that of human cortical bone. However, the compressive strength of the compacts with porosity of that range is slightly lower than that of the human bone. In order to improve the strength, Nomura et al.<sup>(6),(7)</sup> prepared nitrogen added porous Ti compacts and porous Ti-15Mo-5Zr-3Al compacts.

It is important to estimate mechanical properties of such porous compacts for their

material design. Some traditional composite material models such as the self-consistent model<sup>(8),(9)</sup> have been applied to evaluation of them. However, any of the models cannot describe their complicated pore geometry or the geometry of necks connecting spheres, possibly resulting in poor estimation. One of the most powerful methods to predict these properties is the homogenization method<sup>(10)</sup>. In this method, the composite material is assumed to be locally formed by the spatial repetition of very small structures and micro-macro correlation is made by using spatial two scale asymptotic expansions with respect to the parameter which represents a measure of the micro- and macroscopic dimension ratio. However, the critical problem in applying the homogenization method to the random compacts is how we extract a unit cell from an overall random structure and construct a repeated structure. Furthermore, the microstructural modeling is a cumbersome task (e.g., image-based modeling); we need large computational cost.

Kurashige et al.<sup>(11)</sup> proposed a three step simulation method to predict effective elastic moduli of randomly packed identical sphere aggregates. Kato et al.<sup>(12)</sup> extracted a statistical characteristic of the random packing structure from data on the random packing; they also estimated the mechanical properties (effective elastic moduli and elastic wave speeds) by the same evaluation method as that in Kurashige et al.<sup>(11)</sup>. An advantage of this three step simulation method is that statistical characteristic of the microstructure can be evaluated without using another scheme. The statistics is important to understand some relations between the packing structures and their macroscopic characteristics.

The paper by Oh et al.<sup>(4),(5)</sup> above mentioned does not discuss anisotropy of Young's modulus at all. However, Kato et al.<sup>(12)</sup> found that the packing structure is considerably affected by gravity; that is, Young's modulus of the balloon packing in the vertical direction is larger than that in the horizontal directions by approximately 20%. This simulation alludes that the compacts used by Oh et al. in their experiments may have anisotropy.

From this allusion, we can expect that the macroscopic elastic moduli are additionally affected by the uniaxial compaction, leading to stronger anisotropy. In the present paper, we perform a numerical simulation to evaluate the macroscopic elastic properties of randomly-packed sintered spheres. We take into account an effect of the uniaxial compaction in the fabrication process of compacts on macroscopic elastic properties. Following Oh et al.<sup>(5)</sup>, we calculate the macroscopic elastic moduli for the porosity ranging from 25% to 40%; the compacts Oh et al. prepared have the porosity from 32% to 36%.

## 2. Simulation Method of Macroscopic Properties

We use the three step simulation method proposed by Kurashige et al.<sup>(11)</sup> to obtain the effective elastic moduli of a randomly packed sphere aggregate; the simulation methods are schematically shown in Fig. 1.

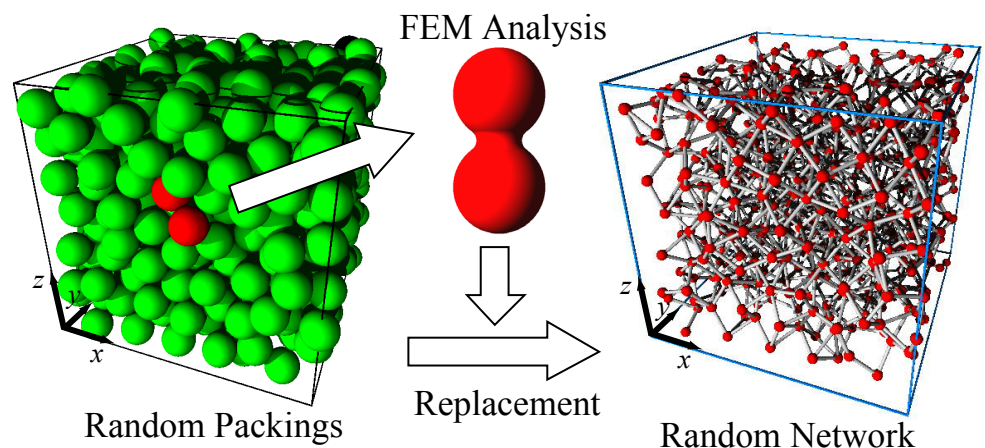


Fig. 1 Illustration of simulation method

First, to generate a structural model of sphere aggregates, we carry out the random packing simulation of sequential accumulation method of identical spheres into a virtual box, together with use of periodic boundary conditions and random ups and downs of the box floor level to avoid packing regularity. After the completion of packing, we make a proportional reduction of distances between sphere centers only in the compaction direction, made to coincide with the gravity direction in sintering, to geometrically express the compaction by uniaxial pressure.

Next, we extract a pair of connected spheres from the packing and regard it as a spring with six degrees of freedom: one for elongation and torsion and two for bending and shearing. Spring constants of the pair of spheres, depending on the reduction of the distance and the mass addition around the neck to express the sintering, are estimated by the finite element analysis.

Finally, we carry out tensile and shear tests of a “random network” of springs, with rigid hinges, of six degrees of freedom with the spring constants already estimated by the finite element analysis. From these tests, we obtain average tensile and shear stress and the average strain resulting from the applied load. Thus, the desired macroscopic Young’s and shear moduli and Poisson’s ratios are determined.

### 3. Geometrical Model of Compacted Sphere Aggregate

#### 3.1 Equation of motion

To generate a geometrical model of porous compacts prepared by powder sintering in a computer, we carry out a random packing simulation. We sequentially throw identical spherical particles with diameter  $D$  from random positions into a box. For the sake of simplicity, we assume that a falling particle is subjected to only gravity and forces from resting particles when collided with them. Thus, the motion equation of the particle can be expressed as follows:

$$c \frac{dx}{dt} = \sum k \Delta d - mg \mathbf{k}, \quad (1)$$

where  $x$  is the position vector of a falling sphere’s center,  $\mathbf{k}$  is the unit vector along the  $z$  axis and  $\Delta d$  is the overlapping depth vector of the particle in collision with another still one. Summation notation  $\sum$  is over the number of all particles in contact with the one under consideration. Notations  $c$ ,  $k$ ,  $m$  and  $g$  are the viscosity constant, the spring constant between two particles in collision, the mass of each sphere and the gravitational acceleration, respectively.

We use the Runge-Kutta-Gill method to solve the three coupled differential equations. In running our program, we use the following non-dimensional numerical values with spherical particle diameter  $D$  as a reference length: time increment  $\Delta T = \Delta t / (mg / cD) = 1.0 \times 10^{-3}$ , spring constant  $K = Dk / (mg) = 1.0 \times 10^3$  and small parameter  $\varepsilon = 1.0 \times 10^{-7}$ ; the last parameter will be used to judge if the sphere rests or not.

Consider a virtual box of  $0 \leq x \leq B$ ,  $0 \leq y \leq B$ ,  $0 \leq z \leq H$  ( $B < H$ ). We do not stop introducing particles until the region  $0 \leq x \leq B$ ,  $0 \leq y \leq B$ ,  $0 \leq z \leq 1.5B$  is completely filled with particles. We continue the particle introduction up to  $z = 1.5B$  because we need the margin for compaction. We adopt box sizes  $B/D = 16$  and five runs are made with five different sets of pseudorandom numbers. We use the periodic boundary conditions and displace the floor up and down in order to avoid packing regularity on its walls and floor, respectively. These random numbers are generated by the algorithm of Whichmann and Hill<sup>(13)</sup>

#### 3.2 Modeling of compaction

Several mechanisms can be involved in powder compaction processes<sup>(14),(15)</sup>: rearrangement and densification of particles, corruption of large voids, and plastic

deformation of particles. All these mechanisms are connected with each other and affected by friction between particles, adhesion of particles and so on; it is difficult to predict them and their connection as well as various affecting factors. Therefore, we will not simulate all this process. Furthermore, we need not know the whole densification process; we need only the microgeometry resulting from random packing and compaction. To describe the compacted geometry, we introduce a new scaled coordinate of each sphere center as follows:

$$Z_i = (1 - \beta)z_i, \quad (2)$$

where  $z_i$  and  $Z_i$  are the  $z$ -coordinate of  $i$ -th sphere center before and after compaction, respectively, and  $\beta$  is the coefficient describing degree of the compaction, varying from 0.0 to 0.2 with 0.01 increment;  $\beta = 0.0$  means no compaction. It must be noted that each sphere remains spherical in spite of the center coordinate scaling.

The compaction modeled in such a way leaves overlapping of spheres, so that each neck resulting from the overlapping has a different diameter. To model the sintering, we add some mass around all necks so as to give the same meniscus radius to all the necks.

Finally, we extract a cubic region  $B \times B \times B$  from a scaled region of the original  $0 \leq X \leq B$ ,  $0 \leq Y \leq B$ ,  $0 \leq Z \leq 1.5B$ . We obtain 105 samples in total (5 samples times 21 scales), for each of which a list of the center coordinates of all resting particles is prepared. These lists will be used to obtain the macroscopic elasticity of compacted, sintered particles later on.

#### 4. Finite Element Analysis of Spring Constants of Sintered Pair

##### 4.1 Model of finite element analysis

In powder sintering, necks are created by mass diffusion around the overlaps made by the artificial reduction in sphere-center distances; the necks grow with sintering time. In order to present this sintered geometry, we add around the overlaps some mass of the same substance as that of the spheres; the added volume is that bounded by the two contact spheres and a torus touching both of them, as shown in Fig. 2. Although the volume reduction by the compaction and the volume addition by the sintering seem to violate the mass conservation, this is not the case because the macroscopic elastic modulus depends only on shape or geometry but not on dimension; that is, the similarity law holds for the elastic modulus. The geometry of the two compacted and sintered spheres can be adjusted to the real one by adjusting the two independent parameters of compaction and sintering degrees, which will be defined just below.

In Fig. 2,  $R$  is the radius of the sphere,  $r_0$  the meniscus radius representing sintering degree,  $h$  the overlapping depth of a sphere pair and  $\Theta$  the sintering degree angle.

The overlapping volume and added volume per contact point can be analyzed by simple geometrical consideration and the results are as follows:

$$\frac{V_{lap}}{2\pi R^3} = \frac{1}{3} \left( \frac{\Delta h}{R} \right)^2 \left( 3 - \frac{\Delta h}{R} \right), \quad (3)$$

$$\begin{aligned} \frac{V_{add}}{2\pi R^3} = & - \left( 1 - \frac{\Delta h}{R} \right) \left( \frac{1 - \cos \Theta - \Delta h/R}{\cos \Theta} \right)^2 \left( 1 + \sin^2 \Theta + \tan \Theta \left( \frac{\pi}{2} - \Theta \right) \right) \\ & + \left( 1 - \frac{\Delta h}{R} \right) \left( \frac{1 - \cos \Theta - \Delta h/R}{\cos \Theta} \right)^2 \tan \Theta \left( 1 - \cos \Theta - \frac{\Delta h}{R} \right) \\ & - \frac{\Delta h}{R} \left( 2 - \frac{\Delta h}{R} \right) \left( 1 - \cos \Theta - \frac{\Delta h}{R} \right) \end{aligned} \quad (4)$$

In what follows, we will adopt the angle  $\Theta$  or the normalized meniscus radius  $r_0/R$  as a parameter of the sintering degree.

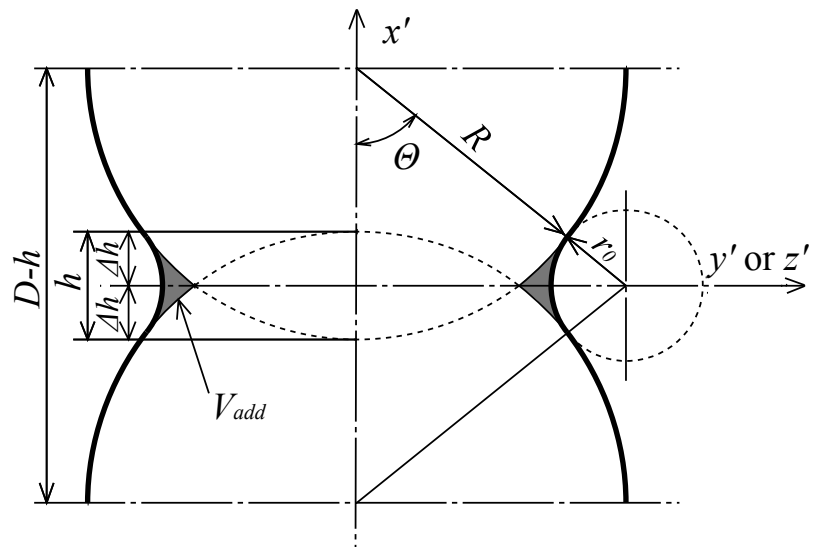


**Fig. 2 Geometry of two compacted spheres with added volume (neck)**

#### 4.2 Results of finite element analysis

The spring has six degrees of freedom: one for elongation and torsion, and two for bending and shearing. The spring constants are defined in the same manner as in the conventional structural analysis. Consider an hourglass shape of the two sintered half spheres shown together with the local coordinate system  $(x', y', z')$  in Fig. 2. We fix its one end and give some generalized displacement on the other end; then we calculate the corresponding generalized forces, which provide the required spring constants. As a function of overlapping depth  $h/D$ , we can obtain  $K_{ex'}$  and  $M_{tx'}$  for axial elongation  $u_{x'} = 1 \times 10^{-5} D$  and torsional angle  $\theta_{x'} = 1 \times 10^{-2}$ , respectively;  $K_{bx'}$  and  $M_{bz'}$  for bending angle and  $K_{sy'}$  and  $M_{sz'}$  for lateral displacement. With respect to these notations,  $K$  and  $M$  correspond to the associated force and moment (or torque); the first subscript represents the deformation modes, while the second one describes the displacement direction or rotation axis. Notice that  $K_{sz'} = K_{sy'}$ ,  $M_{sy'} = M_{sz'}$  and  $K_{bx'} = K_{by'}$  because of geometrical axisymmetry.

We employ the triangular ring elements. Numbers of nodes and elements are 6137 and 11942, respectively, for the largest meshes, while the finest mesh model contains 7580 nodes and 14788 elements. All the finite element analysis has been carried out setting the Poisson's ratio of the particle material to 0.25.

All spring constants normalized by Young's modulus of particle substance  $E_s$  versus the overlapping depth  $h/D$  are given in Figs. 3a to 3d with various radius ratios  $r_0/R$  ranging from 0.0 to 0.2 with their increment being 0.04. Figures 3a and 3b show  $K_{ex'}$  for the axial elongation and  $M_{tx'}$  for the torsion, respectively. Figures 3c and 3d depict  $K_{bx'}$  and  $M_{bz'}$  for the bending. We omit  $K_{sy'}$  and  $M_{sz'}$  for the lateral displacement with no slope at the end (shearing), respectively, because of their similar tendency to the bending. For  $r_0/R = 0.0$ , the spring constants are zero for  $h/D = 0.0$  because of the point contact. The spring constants monotonically increase with increasing overlapping depth  $h/D$ . For  $r_0/R \geq 0.04$ , these spring constants almost linearly increase with increasing overlapping depth related to the compaction. The larger  $r_0/R$ , the larger the spring constants. Notice that  $K_{bx'} = M_{sz'}$  because of the reciprocal relation. We confirmed that these spring constants numerically satisfy this relation.

These spring constants will be used to evaluate the macroscopic elastic moduli of the aggregate in the next section.

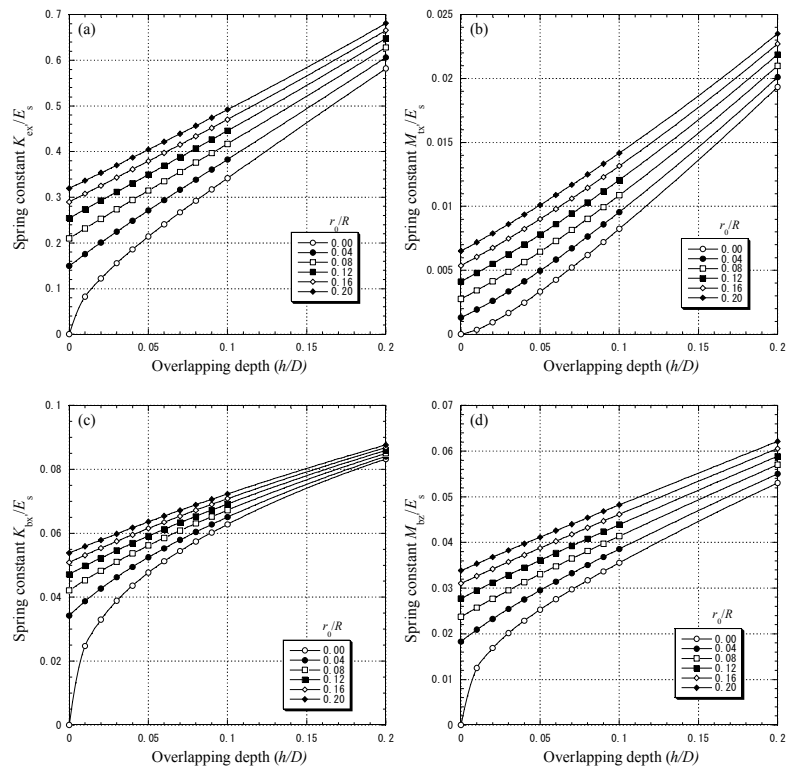


Fig. 3 Spring constants versus sintering degree angle for (a) elongation; (b) torsion; (c) & (d) bending

## 5. Macroscopic Elastic Moduli of Compacted Particles

### 5.1 Simulation method

We will carry out numerical tensile and shear tests of a “random network” of springs, with rigid hinges, of six degrees of freedom with the estimated spring constants. Length of each spring in the networks is different from each other due to the compaction. To carry out the tests, we express the spring constants as follows:

$$\frac{K}{E_s} = C_0 \left( \frac{h}{D} \right)^{C_1} + C_2 \left( \frac{h}{D} \right)^{C_3} + C_4, \quad (5)$$

where  $C_0$ ,  $C_2$  and  $C_4$  are the constants to be determined by the least square method after the exponents  $C_1$  and  $C_3$  of  $(h/D)$  are fixed by the trial and error method. We calculate all the overlapping depths in the random network from the coordinates of sphere centers. Thus, from the regression curve in Eq. (5), we can obtain the spring constants of any spring required in analyzing the network.

The random network is a mechanical model of the compacted, sintered sphere aggregate. The model might be satisfactory if deformation of each hourglass-shaped spring is concentrated around its neck. This concentrated deformation for all springs would account for the overall deformation of the sintered aggregate. To confirm this is the case, we calculate strain energy density within the particle pair from the above finite element analysis. Although the results are not shown here, it is seen that the high density region is near the sintered portion. This argument reveals that both ends of the hourglass-shaped spring, which are far from the neck or sintered portion, are little deformed and play a roll of the rigid hinge.

We carry out both the tensile test in the  $x$ ,  $y$  and  $z$  directions and the shear tests in the  $x-y$ ,  $x-z$  and  $y-z$  planes of the networks. From the tensile tests, we obtain the macroscopic Young's moduli  $E_x^*$ ,  $E_y^*$  and  $E_z^*$  and Poisson's ratios  $\nu_{xy}$ ,  $\nu_{xz}$ ,  $\nu_{yx}$ ,  $\nu_{yz}$ ,  $\nu_{zx}$ ,  $\nu_{zy}$ . Furthermore, we obtain  $G_{xy}^*$ ,  $G_{xz}^*$  and  $G_{yz}^*$  from the shear tests.

We use a program for the 3D structural analysis, which is borrowed from a textbook<sup>(16)</sup>,

to simulate both of the tests. We assign tensile (or shearing) forces at the nodes within uppermost and lowermost (and rightmost and leftmost) layers with thickness of  $D$  within the box for random packing. Magnitude of the forces is determined so that their resultant forces (moments) be in equilibrium with the applied tensile (shear) forces  $P$  and their moments vanish about the three axes passing through the center of an arbitrarily selected particle. Furthermore, we fix this particle (that is, give no displacement and no rotation) to avoid any rigid displacement and rotation of the whole network of springs. Before running the program, we re-number all spheres (or all nodes) so as to minimize the band width of the total stiffness matrix for each sample.

We obtain average tensile (or shear) stresses from the applied load and determine the average strains by averaging ratios of the respective displacement component of each particle within the outermost layers of thickness  $D$  to the corresponding separation from a reference particle over all particles within the layers. Thus, the desired macroscopic Young's moduli, shear moduli and Poisson's ratios are determined by the respective definitions.

## 5.2 Young's and shear moduli

Figures 4 and 5 respectively show macroscopic Young's moduli and shear moduli versus the total porosity in the compacted, sintered state. Although we have calculated all these moduli for all samples, we will present only graphs for Sample 1, because we can see little difference among the samples for all compaction degrees. In all the figures, the ordinate presents their macroscopic Young's moduli  $E^*$  or shear moduli  $G^*$  normalized by Young's modulus of sphere substance  $E_s$ ;  $n_0/R$  is adopted as a geometrical parameter.

Figures 4a and 4b show the porosity dependence of Young's moduli  $E_x^*/E_s$  and  $E_z^*/E_s$ , while Figs. 5a and 5b imply  $G_{xy}^*/E_s$  and  $G_{xz}^*/E_s$ . Each marker on an individual curve in both the figures corresponds to the nondimensional sintering degree radius  $n_0/R$  ranging from 0.0 to 0.2 at intervals of 0.04 and progress toward the right on the curve makes the sintering degree low.

We examine dependence of the elastic moduli on the degree of sintering and compaction; for each constant compaction degree, the smaller the degree of sintering is, the smaller the elastic moduli. Increases in the compaction degree raise the curves as a whole, especially more for the higher degree of sintering. They also shift the curves toward lower porosity as a whole, because the packings become dense.

These moduli depend on the compaction and sintering degree in a very complicated manner. Comparing Figs. 4a and 4b,  $E_z^*$  is larger than  $E_x^*$  by roughly 20% to 40% for over the entire region of porosity. Similarly,  $G_{xy}^*$  is larger than  $G_{xz}^*$  by roughly 30% to 40% as shown in Figs. 5a and 5b. Furthermore, we can numerically confirm, although not shown, that  $E_x^* = E_y^*$  and  $G_{xz}^* = G_{yz}^*$ . These observations show again that the simulated packing structure is of transverse isotropy, whose isotropy plane lies in the  $x-y$  plane and whose axis coincides with the  $z$  axis.

Finally, let us focus on the effect of the compaction on the degree of anisotropy. We consider the case of no added mass in which  $n_0/R = 0.0$  to take out only influence of the compaction. In this case, the macroscopic Young's modulus in the  $Z$  direction  $E_z^*/E_s$  is roughly 20% larger than that in the  $x$  direction  $E_x^*/E_s$  for  $\beta = 0.02$  (almost no compaction), but roughly 40% larger for  $\beta = 0.20$  (considerable compaction). Thus, roughly speaking, the increase in Young's modulus due to the compaction is 20%. Note that we select  $\beta = 0.02$ , not only  $\beta = 0.0$ , because stiffness of  $\beta = 0.0$  is zero at  $n_0/R = 0.0$ .

Young's moduli  $E_z^*$  and  $E_x^*$  and shear modulus  $G_{xz}^*$  and  $G_{xy}^*$  depend on both the compaction and sintering degrees in a very complicated manner. Therefore, it is important for practical purposes to express all the elastic moduli in terms of expressions of the two geometrical parameters  $n_0/R$  and  $\beta$ . The expressions are determined by the conventional least square method from the data of all five samples as follows:

$$\frac{E_x^*}{E_s} = \left( -4.3 \times 10^{-2} - 1.76 \times 10^{-1} \left( \frac{r_0}{R} \right)^{0.2} + 7.84 \times 10^{-1} \left( \frac{r_0}{R} \right)^{0.4} \right) \beta^{0.1} + \left( 4.32 \times 10^{-1} - 9.91 \times 10^{-3} \left( \frac{r_0}{R} \right)^{0.2} - 3.21 \times 10^{-1} \left( \frac{r_0}{R} \right)^{0.4} \right) \beta^{0.3} \quad (6)$$

$$\frac{E_z^*}{E_s} = \left( -2.27 \times 10^{-2} - 2.95 \times 10^{-1} \left( \frac{r_0}{R} \right)^{0.2} + 1.08 \left( \frac{r_0}{R} \right)^{0.4} \right) \beta^{0.1} + \left( 5.46 \times 10^{-1} - 2.83 \times 10^{-3} \left( \frac{r_0}{R} \right)^{0.2} - 1.22 \left( \frac{r_0}{R} \right)^{0.4} \right) \beta^{0.3} \quad (7)$$

$$\frac{G_{xy}^*}{E_s} = \left( -1.45 \times 10^{-2} - 6.97 \times 10^{-2} \left( \frac{r_0}{R} \right)^{0.2} + 3.22 \times 10^{-1} \left( \frac{r_0}{R} \right)^{0.4} \right) \beta^{0.1} + \left( 1.74 \times 10^{-1} - 1.4 \times 10^{-3} \left( \frac{r_0}{R} \right)^{0.2} - 1.62 \times 10^{-1} \left( \frac{r_0}{R} \right)^{0.4} \right) \beta^{0.3} \quad (8)$$

$$\frac{G_{xz}^*}{E_s} = \left( -1.1 \times 10^{-2} - 1.4 \times 10^{-1} \left( \frac{r_0}{R} \right)^{0.2} + 5.06 \times 10^{-1} \left( \frac{r_0}{R} \right)^{0.4} \right) \beta^{0.1} + \left( 2.19 \times 10^{-1} - 1.17 \times 10^{-1} \left( \frac{r_0}{R} \right)^{0.2} - 4.98 \times 10^{-1} \left( \frac{r_0}{R} \right)^{0.4} \right) \beta^{0.3} \quad (9)$$

All the equations are valid for  $0.0 \leq r_0/R \leq 0.2$  and  $0.02 \leq \beta \leq 0.2$  to within 5.5%.

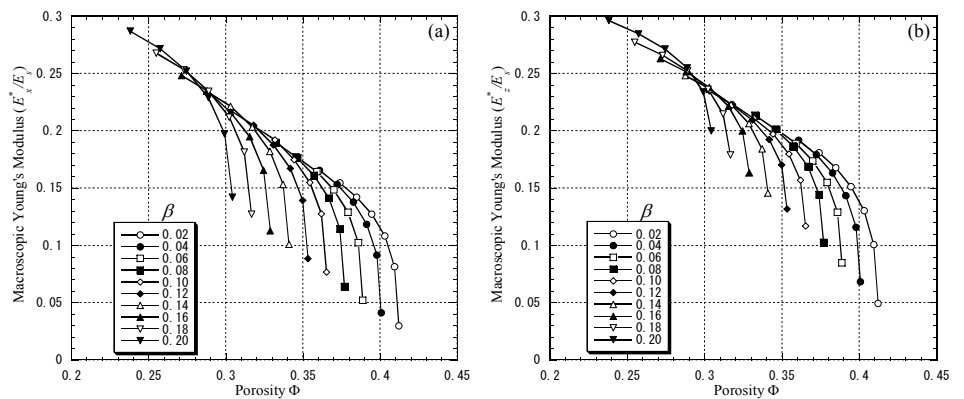


**Fig. 4** Young's moduli versus porosity: (a) in isotropy plane and (b) along anisotropy axis

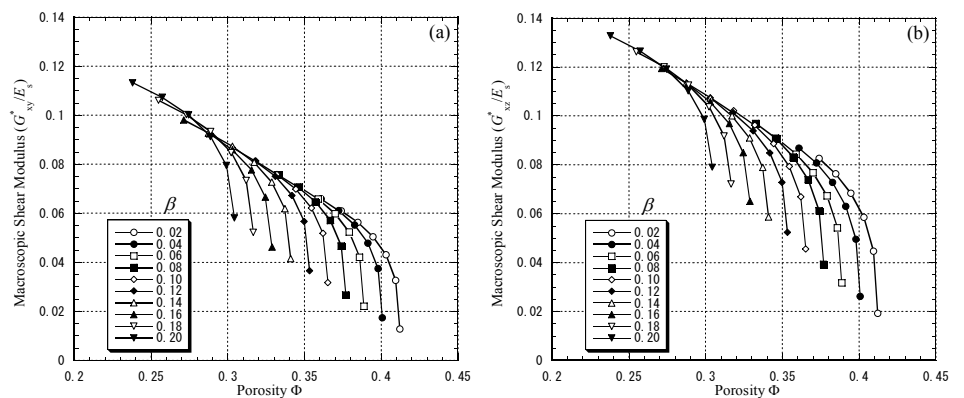


**Fig. 5** Shear moduli versus porosity: (a) in isotropy plane and (b) between isotropy plane and anisotropy axis

### 5.3 Poisson's ratio

Behavior of Poisson's ratios is a little more complicated than that of Young's and shear moduli. Although the Poisson's ratios have large scatterings among the samples, we also show only the result of the Sample 1.

The behavior of Poisson's ratios,  $\nu_{xy}$ ,  $\nu_{xz}$  and  $\nu_{zx}$  against the total porosity for various compaction degree  $\beta$  ranging from 0.0 to 0.2 with their increment being 0.02 are shown in Figs. 6a-c, respectively;  $\nu_{xy}$  means Poisson's ratio in the isotropy plane;  $\nu_{xz}$  denotes the contraction ratio in the  $z$  axis under uniaxial tension in the  $x$  direction, while  $\nu_{zx}$  the one in the  $x$  axis under  $z$  tension. All the estimation of all Poisson's ratios is based on the definitions described here; in other words, not on some relations among other elastic moduli estimated.

The macroscopic Poisson's ratio obtained is smaller than that of the powder substance  $\nu = 0.25$ . It seems to be a general tendency that Poisson's ratio of porous materials is smaller than that of the original material; a few papers report on this topic<sup>(17)</sup>.

In Fig. 6, it can be seen that the dependence of Poisson's ratios on the porosity is similar to that of Young's and shear moduli. The Poisson's ratios decrease with decreasing sintering degree angle for each compaction degree. Poisson's ratio in the isotropy plane  $\nu_{xy}$  is the smallest, while  $\nu_{zx}$  is the largest;  $\nu_{xz}$  lies between them.

It is interesting that Poisson's ratio  $\nu_{zx}$  for all the compaction degrees sharply ascends with an approach of porosity to the non-sintered state, while  $\nu_{xy}$  and  $\nu_{xz}$  do not. Although the similar ascent is seen for the non-compacted solid sphere aggregates obtained by Kato et al.<sup>(12)</sup>, we have not found any unified reason to justify this ascent yet; more precise numerical calculation or theoretical consideration might be needed.

We have already given the formulae to estimate the four elastic moduli. If we select  $\nu_{zx}$  as a final one from the five independent moduli for transversely isotropic media, we can express its dependence on  $n/R$  and  $\beta$  as follows:

$$\begin{aligned} \nu_{zx} = & \left( 4.22 \times 10^{-1} - 1.66 \left( \frac{n}{R} \right)^{0.2} + 1.99 \left( \frac{n}{R} \right)^{0.25} \right) \beta^{0.1} \\ & + \left( -2.13 \times 10^{-1} - 2.06 \left( \frac{n}{R} \right)^{0.2} - 2.55 \left( \frac{n}{R} \right)^{0.25} \right) \beta^{0.3} \end{aligned} \quad (10)$$

This equation describes the results for  $0.04 \leq n/R \leq 0.2$  and  $0.02 \leq \beta \leq 0.2$  to within 10% in all cases. Note that the lower limit of the sintering degree is 0.02 to avoid the rapid ascent in the ratio in approaching the non-sintered state.

For the transverse isotropy in elasticity, the reciprocal relations

$$\frac{\nu_{xz}}{E_x^*} = \frac{\nu_{zx}}{E_z^*}, \quad \frac{\nu_{yz}}{E_y^*} = \frac{\nu_{zy}}{E_z^*} \quad (11)$$

must be fulfilled. Poisson's ratio  $\nu_{xz}$  can be determined from the first relation. In addition,  $\nu_{yz} = \nu_{xz}$  and  $\nu_{zy} = \nu_{zx}$ . We have numerically confirmed that the present results almost satisfy these relations.

Poisson's ratio  $\nu_{xy}$  can be expressed in terms of  $E_x^*$  and  $G_{xy}^*$  as

$$\nu_{xy} = \frac{E_x^*}{2G_{xy}^*} - 1. \quad (12)$$

However, Poisson's ratios  $\nu_{xy}$  calculated by Eq. (12) considerably differ from the simulated ones. If  $G_{xy}^*$  deviates by  $\pm 5\%$  in Eq. (12),  $\nu_{xy}$  varies as much as 30%. Thus, we cannot use Eq. (12) to determine Poisson's ratio  $\nu_{xy}$ . Instead, Poisson's ratio  $\nu_{xy}$  can be obtained from the following expression in terms of  $n/R$  and  $\beta$  obtained in a similar manner as that for Eq. (10):

$$\nu_{xy} = \left( 2.17 \times 10^{-1} + 3.08 \times 10^{-1} \left( \frac{r_0}{R} \right)^{0.2} - 3.05 \times 10^{-1} \left( \frac{r_0}{R} \right)^{0.4} \right) \beta^{0.1} + \left( -1.01 \times 10^{-1} - 4.3 \times 10^{-1} \left( \frac{r_0}{R} \right)^{0.2} + 5.52 \times 10^{-1} \left( \frac{r_0}{R} \right)^{0.4} \right) \beta^{0.3} \quad (13)$$

The equation describes the results for  $0.02 \leq r_0 / R \leq 0.2$  and  $0.02 \leq \beta \leq 0.2$  to within 10% in all cases.

We have determined the in-plane shear modulus  $G_{xy}^*$  from the shear tests. However, we can calculate  $G_{xy}^*$  from only the tensile test using Eq. (12). The results are in good agreement with those from the shear test to within  $\pm 5\%$ .

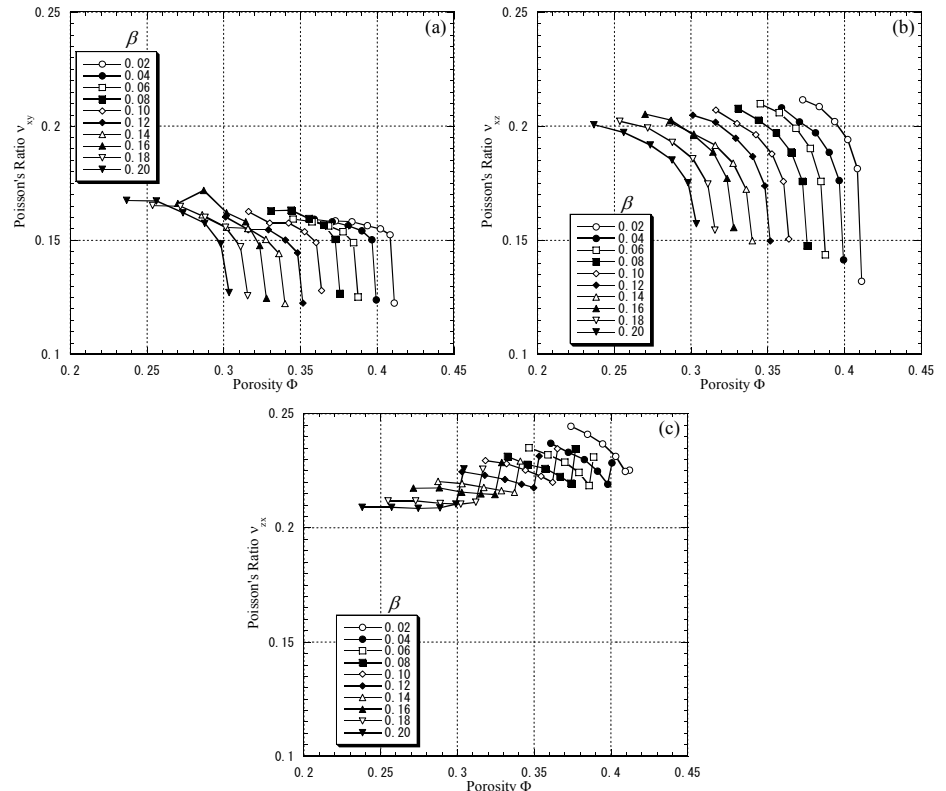


**Fig. 6 Three independent Poisson's ratios versus porosity: (a)  $\nu_{xy}$ , (b)  $\nu_{xz}$  and (c)  $\nu_{zx}$ , for  $r_0 / R$  ranging from 0.0 to 0.2**

#### 5.4 Comparison with experimental data

We compare the present macroscopic Young's moduli with the experimental results obtained by Oh et al.<sup>(5)</sup> for artificial bone made of Ti. All markers in Fig. 7 show the simulated macroscopic Young's moduli in the  $z$  direction. The solid straight line implies the line based on the experimental data in Ref. (5) and the slashed region shows the range of Young's modulus of human cortical bone<sup>(4)</sup>. If the simulated Young's moduli of sintered and compacted aggregates of spheres fall in this range, those aggregates could be utilized as implants with respect to their rigidity.

We observe from the SEM micrograph in Ref. (4) that the microgeometry of sintered porous Ti compacts is close to that of the present model with  $r_0 / R = 0.0$ . Thus, we assume that  $r_0 / R = 0.0$ , when we compare the results with the experimental results<sup>(5)</sup>. (Note that this assumption of  $r_0 / R = 0.0$  is not always applicable to any other porous compacts because the microgeometry depends on materials and sintering conditions; the other model may be needed.)

It is seen from Fig. 7 that the present macroscopic Young's moduli in the  $z$  direction

depicted by the hollow circles ( $r_0/R = 0.0$ ) are comparable to the experimental one in the dashed region of human cortical bone, supposing that the experimental ones are in the direction of compaction, i.e., in the  $z$  direction. However, the slopes of the both results are considerably different from each other. The following two possible reasons can account for this difference. The results by Oh et al. were approximated by a straight line for the wide range of porosity (from 0% to 40%) but the range corresponding to the human cortical bone is very narrow, so that the slope in this narrow range is not reliable; in addition, data points do not seem sufficient. The second reason comes from the assumption of  $r_0/R = 0.0$ ; we can say that relief of this assumption, i.e., introduction of the slight sintering must make the slope steeper.

On the other hand, we consider another realistic geometrical model of the particle pair; we introduce a restriction that the overlap volume of the particle pair equals the added volume corresponding to the sintering, that is, the mass is conserved in sintering without scaling. We will call this model as a conservation model. Equating Eq. (3) to Eq. (4), we can determine the sintering degree angle  $\Theta$  by iteration.

The result from the conservation model is shown by the hollow crosses connected by a thin solid curve in Fig. 7. Although the mass conservation seems to be realistic, the curve shows a worse agreement with the results of artificial bone by Oh et al.

However, it should be noted that both the hollow circle markers calculated based on the assumption of  $r_0/R = 0.0$  and the hollow crosses connected by a thin solid curve obtained by the mass conservation can be made to fall in the slashed region of Young's moduli of cortical bone by varying the degree of sintering or compaction. The porosity corresponding to the cortical bone ranges from 32% to 37% if the former assumption is adopted.

It may be concluded that the model of  $r_0/R = 0.0$  is better than the mass conservation model in terms of the agreement between the experiment and the simulation; the former is based on the observation of necks by the SEM micrograph. Note that the former model can be made to comply with the mass conservation law by scaling of the whole aggregate.

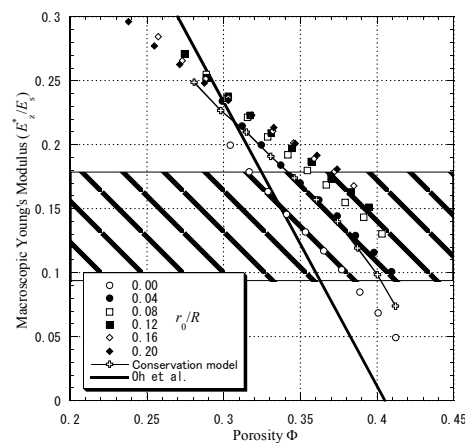


**Fig. 7 Macroscopic Young's moduli versus porosity for  $r_0/R$  ranging from 0.0 to 0.2 and conservation model together with experimental data in Ref. (5); slashed region shows range of Young's modulus of human cortical bone**

## 6. Concluding Remarks

We have numerically evaluated the macroscopic elastic properties of porous compacts prepared by uniaxial pressurization in sintering; the compacts are intended to be used as biomedical implants.

It is found that the compaction by the pressure and the sintering lead to increase in the macroscopic elastic moduli in the pressure direction, which is made to coincide with that of the gravity in packing. It is also found that these moduli are larger than those in the direction normal to the pressure by 20% to 40%. This anisotropy should be considered in using the

present kind of compacts as implants. The elastic moduli for the less sintered compacts whose porosity range from approximately 32% to 37 % fall in those of human cortical bone and are comparable to those of artificial Ti implants.

### Acknowledgements

The authors would like to express their heartfelt thanks to Dr. Naoyuki Nomura, Iwate University, for fruitful discussions on the fabrication method of porous Ti compacts and many others.

### References

- (1) Niinomi M. Fatigue Performance and Cyto-Toxicity of Low Rigidity Titanium Alloy, Ti-29Nb-13Ta-4.6Zr, *Biomaterials* Vol. 24 (2003), pp. 2673-2683.
- (2) Spoerke, E.D. et al., A Bioactive Titanium Foam Scaffold for Bone Repair, *Acta Biomaterialia*, Vol. 1 (2005), pp. 523-533.
- (3) Schneider, E. et al., A Comparative Study of the Initial Stability of Cementless Hip Prostheses, *Clin Orthop Relat Res.*, Vol. 248 (1989), pp. 200-209.
- (4) Oh, I.H. et al., Microstructures and Mechanical Properties of Porous Titanium Compacts Prepared by Powder Sintering. *Materials Transactions*, Vol. 43 (2002), pp. 443-446.
- (5) Oh, I.H. et al., Mechanical Properties of Porous Ti Compacts Prepared by Powder Sintering, *Scripta Materialia*, Vol. 49 (2003), pp. 1197-1202.
- (6) Nomura, N. et al., Mechanical Properties of Porous Ti-15Mo-5Zr-3Al Compacts Prepared by Powder Sintering. *Materials Science & Engineering C*, Vol. 25 (2005), pp. 330-335.
- (7) Nomura, N. et al., Fabrication and Mechanical Properties of Porous Co-Cr-Mo Alloy Compacts without Ni Addition, *Materials Transactions*, Vol. 47 (2006), pp. 283-286.
- (8) Wu, T. T., The Effect of Inclusion Shape on the Elastic Moduli of a Two-Phase Material, *International Journal of solids and structures*, Vol. 2 (1966), pp. 1-8.
- (9) Berryman, J. G., Elastic Wave Propagation in Fluid-Saturated Porous Media, *J. Acoust. So. Am.*, Vol. 69 (1981), 416-424.
- (10) Guedes, J.M. and Kikuchi, N., Preprocessing and Postprocessing for Materials Based on the Homogenization Method with Adaptive Finite Element Methods, *Computer Methods in Applied Mechanics and Engineering*, Vol. 83 (1990), pp. 143-198.
- (11) Kurashige, M. et al., Simulated Effective Elastic Moduli and Wave Velocities in Water-Saturated Sintered Glass-Beads, *Acta Mechanica*, Vol. 132 (1999), pp. 177-194.
- (12) Kato, H. et al., Anisotropy in Packing Structure and Elasticity of Sintering Spherical Particles, *JSME International Journal, Series A*, Vol. 45-4 (2002), pp. 585-595.
- (13) Wichmann, B.A. and Hill, I.D., An Efficient and Portable Pseudo-Random Number Generator, *Royal Statistical Society*, Algorithm as 183 (1982), pp. 188-190.
- (14) Martin, C.L. and Bouvard D., Study of the Cold Compaction of Composite Powders by the Discrete Element Method. *Acta Materialia*, Vol. 51 (2003), pp. 373-386.
- (15) Kim, K.T. et al., Densification Behavior of Aluminum Alloy Powder Mixed with Zirconia Powder Inclusion under Cold Compaction, *Materials Science and Engineering A*, Vol. 340 (2003), pp. 41-48.
- (16) Beaufait F.W. et al., *Computer methods of structural analysis*, (1970), Prentice-Hall, Englewood Cliffs.
- (17) George, J., et al., The Elastic Response of a Cohesive Aggregate - a Discrete Element Model with Coupled Particle Interaction, *Journal of the Mechanics and Physics of Solids*, Vol.50 (2002), pp. 2539-2575.